HHS Public Access

Author manuscript

Int J Radiat Oncol Biol Phys. Author manuscript; available in PMC 2022 February 01.

Published in final edited form as:

Int J Radiat Oncol Biol Phys. 2021 February 01; 109(2): 614–625. doi:10.1016/j.ijrobp.2020.09.040.

Fully Balanced SSFP Without an Endorectal Coil for Postimplant QA of MRI-Assisted Radiosurgery (MARS) of Prostate Cancer: A Prospective Study

Jeremiah W. Sanders, PhD[*,†], **Aradhana M. Venkatesan, MD**[‡], **Chad A. Levitt, MD**[§], **Tharakeswara Bathala, MD**[‡], **Rajat J. Kudchadker, PhD**[‖], **Chad Tang, MD**[¶], **Teresa L. Bruno, CMD**[¶], **Christine Starks, CMD**[¶], **Edwin Santiago, CMD**[¶], **Michelle Wells, MS**[§], **Carl P. Weaver, MS**[§], **Jingfei Ma, PhD**[*,†], **Steven J. Frank, MD**[¶]

[*]Department of Imaging Physics, University of Texas MD Anderson Cancer Center, Houston, Texas

[†]Medical Physics Graduate Program, MD Anderson Cancer Center UTHealth Graduate School of Biomedical Sciences, Houston, Texas

[‡]Department of Radiation Oncology, Piedmont Hospital, Atlanta, Georgia

[§]Department of Diagnostic Radiology, University of Texas MD Anderson Cancer Center, Houston, Texas

[‖]Department of Radiation Physics, University of Texas MD Anderson Cancer Center, Houston, Texas

[¶]Department of Radiation Oncology, University of Texas MD Anderson Cancer Center, Houston, Texas

Abstract

Purpose: To investigate fully balanced steady-state free precession (bSSFP) with optimized acquisition protocols for magnetic resonance imaging (MRI)-based postimplant quality assessment of low-dose-rate (LDR) prostate brachytherapy without an endorectal coil (ERC).

Methods and Materials: Seventeen patients at a major academic cancer center who underwent MRI-assisted radiosurgery (MARS) LDR prostate cancer brachytherapy were imaged with moderate, high, or very high spatial resolution fully bSSFP MRIs without using an ERC. Between 1 and 3 signal averages (NEX) were acquired with acceleration factors (R) between 1 and 2, with the goal of keeping scan times between 4 and 6 minutes. Acquisitions with R >1 were reconstructed with parallel imaging and compressed sensing (PICS) algorithms. Radioactive seeds were identified by 3 medical dosimetrists. Additionally, some of the MRI techniques were

Corresponding author: Jeremiah W. Sanders, PhD; jsanders1@mdanderson.org.

Disclosures: S.J.F. is a cofounder of C4 Imaging, has ownership interests in the company, and has US and international patents licensed to C4 Imaging. J.M. has US patents licensed to Siemens Healthineers and is a consultant for C4 Imaging.

The authors cannot make the images used in this study publicly available due to institutional policies. Computer code used to perform the image reconstructions can be found at https://github.com/jeremiahws/pulse_seq_dev.

Supplementary material for this article can be found at https://doi.org/10.1016/j.ijrobp.2020.09.040.

implemented and tested at a community hospital; 3 patients underwent MARS LDR prostate brachytherapy and were imaged without an ERC.

Results: Increasing the in-plane spatial resolution mitigated partial volume artifacts and improved overall seed and seed marker visualization at the expense of reduced signal-to-noise ratio (SNR). The reduced SNR as a result of imaging at higher spatial resolution and without an ERC was partially compensated for by the multi-NEX acquisitions enabled by PICS. Resultant image quality was superior to the current clinical standard. All 3 dosimetrists achieved near-perfect precision and recall for seed identification in the 17 patients. The 3 postimplant MRIs acquired at the community hospital were sufficient to identify 208 out of 211 seeds implanted without reference to computed tomography (CT).

Conclusions: Acquiring postimplant prostate brachytherapy MRI without an ERC has several advantages including better patient tolerance, lower costs, higher clinical throughput, and widespread access to precision LDR prostate brachytherapy. This prospective study confirms that the use of an ERC can be circumvented with fully bSSFP and advanced MRI scan techniques in a major academic cancer center and community hospital, potentially enabling postimplant assessment of MARS LDR prostate brachytherapy without CT.

Introduction

Routine postimplant imaging after low-dose-rate (LDR) prostate brachytherapy relies on computed tomography (CT). Although CT provides high contrast of implanted radioactive seeds,[1,2] it is limited by its poor soft-tissue contrast, making delineation of the prostate and surrounding normal structures difficult. Significant streak artifacts caused by photon starvation further complicate the ability to delineate the relevant pelvic anatomy for postimplant assessment.

In contrast to CT, magnetic resonance imaging (MRI) provides high soft-tissue contrast.[3] The soft-tissue contrast in MRI can be prescribed by the selection and subsequent optimization of the pulse sequence selected for imaging. However, implanted radioactive seeds, because of their metallic construction, do not produce any MR signal. This causes the seeds to appear as signal voids within the MRI, making their localization in postimplant quality assessment (QA) challenging. Some groups have developed multimodality techniques for postimplant QA, whereby both CT and MRI are acquired and used to perform dosimetric assessment.[4–7] Physicians have used these techniques for many years for postimplant QA, but they have the drawback that 2 image sets from different imaging modalities must be acquired and coregistered.

Researchers recently developed the ability to use MRI alone to simultaneously image implanted radioactive seeds and the pelvic anatomy with a single MRI pulse sequence for MRI-assisted radiosurgery (MARS) of prostate cancer with LDR prostate brachytherapy.[8] This technique relies on the use of implanted seed markers, which produce positive MRI signal and act as functional spacers between the radioactive seeds, enabling seed localization for postimplant QA.[9,10] These images are typically acquired with an endorectal coil (ERC), used to improve the signal-to-noise ratio (SNR) to a level that is adequate to delineate anatomic boundaries along with the implanted radioactive seeds and seed markers. However,

the use of an ERC has several disadvantages including reduced patient tolerance, increased cost, reduced clinical throughput, and coil-related image artifacts.

Imaging without an ERC inherently decreases the SNR, which can reduce the ability to perform accurate postimplant QA. Furthermore, high spatial resolution is required to adequately resolve implanted seed markers for assistance with seed localization. Increasing spatial resolution comes with a further reduction in SNR. A previous retrospective study demonstrated the feasibility of using combined parallel imaging and compressed sensing (PICS) to accelerate postimplant MRI without significant noise amplification, potentially enhancing SNR via the acquisition of multiple signal averages.[11] This technique could help compensate for the SNR lost in imaging without an ERC and with high spatial resolution (reduced voxel size), but it has yet to be investigated in a prospective clinical setting.

The present study prospectively investigates techniques to acquire high-quality prostate MRIs for postimplant QA without an ERC for MARS of prostate cancer with LDR brachytherapy. We investigated the impact of increasing spatial resolution on seed marker visualization. We further investigated the use of PICS to acquire multiple signal averages and boost the SNR without significantly increasing scan times. Additionally, we demonstrated the first translation of some of these techniques from an academic setting to a community hospital.

Materials and Methods

This prospective study was conducted under a Health Insurance Portability and Accountability Act–compliant and Institutional Review Board–approved protocol at The University of Texas MD Anderson Cancer Center (MDACC), and a process improvement project at Piedmont Atlanta Hospital (PAH). Informed patient consent was acquired before imaging at MDACC.

Patient inclusion

Twenty male patients at MDACC and 3 male patients at PAH, with confirmed prostate cancer were selected for this study. All patients underwent MARS with a stranded LDR brachytherapy technique. Radioactive seed models included Pd-103 (Theragenics, Theraseed, Buford, GA) and I-125 (IsoAid, Advantage I-125, Port Richey, FL). Both the Pd-103 and I-125 seeds were 4.5 mm in length and 0.8 mm in diameter. The radioactive seeds were stranded with positive MR signal seed markers (Sirius, C4 Imaging, Houston, TX) serving as functional spacers.[9,10] The seed markers were 5.5 mm in length and had outer and inner diameters of 0.8 mm and 0.5 mm, respectively. All postimplant MRI scans at MDACC were performed the day after the implant surgery. The postimplant MRI scans at PAH were performed on the same day of the implant procedure.

Two patients who were not able to control their leg movement were excluded from the MDACC group because their MRIs showed severe motion artifacts that were unavoidable. A third patient with a prior prostatectomy was also excluded because LDR brachytherapy was performed as salvage treatment to a region in proximity to the prostate bed.

Patient positioning

All MRI scans at MDACC were performed on a Siemens 3T Prisma Scanner (Siemens Healthineers, Erlangen, Germany) operating under the VE11C software version. Patients were positioned feet-first supine in the MRI scanner bore. Two 18-channel external array coils were used for imaging: 1 was positioned posteriorly below the pelvis, and the other was positioned anteriorly above the pelvis. A localizer image was acquired to prescribe the field of view (FOV) for a sagittal T2-weighted image, which was acquired to further refine the center of the FOV about the prostate for the subsequent MRI scans.

Pulse sequence selection

The implanted seed markers were filled with a cobalt dichloride-N-acetylcysteine solution, which has a short T1 and yields positive T1-weighted MRI contrast.[12] Pulse sequences providing T2-weighted MRI contrast are superior to T1-weighted sequences for anatomic imaging. Previously, a T1-weighted spoiled gradient echo sequence and a T2-weighted fast spin echo sequence were used for imaging of seed markers and prostatic anatomy, respectively, for MARS LDR prostate brachytherapy.[13,14] However, prior work has demonstrated the ability to simultaneously image implanted seed markers and anatomic boundaries using fully balanced steady-state free precession (bSSFP) MRI,[8] which provides a mixture of T2-weighted and T1-weighted MRI contrast.

Two variants of the 3-dimensional (3D) fully bSSFP pulse sequence exist on the Siemens platform. The first variant is TrueFISP (GE: FIESTA; Phillips: Balanced-FFE), the traditional implementation of fully bSSFP, in which the gradients along all 3 axes are balanced during each repetition time (TR). As a result, this sequence yields the highest SNR efficiency among all clinical sequences.[15] This characteristic is beneficial for prostate imaging without an ERC, in which the prostate is in the center of the FOV and far from the external array coils. TrueFISP is also very fast because it has a short TR, which is helpful for managing motion artifacts. TrueFISP is highly susceptible to magnetic field inhomogeneity, which causes severe banding artifacts in the images. The second variant, constructive interference in steady-state (CISS) (GE: FIESTA-C), mitigates these artifacts by acquiring 2 TrueFISP acquisitions with phase cycling and combining the 2 images to reduce the artifacts.[16]

The 3D CISS sequence was selected for all postimplant MRI scans. Moderate (0.586 × 0.586 mm, interpolated to 0.293 × 0.293 mm), high (0.469 × 0.469 mm, interpolated to 0.234 × 0.234 mm), and very high (0.390 × 0.390 mm, interpolated to 0.195 × 0.195 mm) in-plane spatial resolution scans were acquired. Acquisition of a fully sampled single signal average (NEX) was performed, followed by a second accelerated acquisition (acceleration factor, R = 2) with either NEX = 2 or NEX = 3. The scan time for each series was kept to approximately 4 to 6 minutes to minimize motion artifacts. Representative scan parameters are summarized in Table 1.

Sampling trajectories

Arbitrary k-space sampling was incorporated into the 3D CISS pulse sequence (Supplementary Fig. E1). The sequence was written to sample k-space lines in accordance

with a binary sampling mask. For a given k_y line, the sequence cycles through k_z lines and samples those that are true in the binary sampling mask. The same sampling pattern was used for both phase-cycled k-space acquisitions of the CISS sequence. Four k-space sampling patterns with R = 2 were investigated, consisting of random, pseudorandom Poisson disk,[17–19] and both single- and multiphase encoding GRAPPA accelerations.[20] The pseudorandom Poisson disk sampling patterns were created using the Berkeley Advanced Reconstruction Toolbox (BART).[21–23] The sampling pattern yielding the highest seed marker conspicuity (particularly sharpness) and anatomy delineation was identified through subjective evaluation in 3 patient MRIs (not included in the prospective cohort) and used for all patient examinations.

Image reconstruction

The fully sampled acquisitions were reconstructed online using the default image reconstruction pipeline that Siemens implemented for the CISS sequence. The accelerated acquisitions were reconstructed offline using the Siemens image calculation environment (ICE). The k-space data of the accelerated acquisitions were reconstructed with parallel imaging (PI) and compressed sensing (CS) algorithms incorporated into BART using the process described subsequently.

First, the k-space data were exported from the scanner in the TWIX data format (.dat binary files). These data files were read using an open-source parsing function (mapVBVD.m)[24] in Matlab v2019a (The MathWorks, Natick, MA). Coil sensitivity maps were estimated from the central fully sampled regions of k-space using BART (24 × 24 region, kernel size of 6). Each accelerated acquisition was reconstructed using both eigenvector-based iterative self-consistent parallel imaging (ESPIRiT) and L1-ESPIRiT algorithms.[25] For the L1-ESPIRiT reconstructions, the regularization term λ was set to 0.003, and a wavelet transform was used as the sparsifying transform.[11] More information about the parameters for these reconstructions can be found in previous work.[11] Copies of the measurement data files were made, and the reconstructed k-space data were written back to them to create synthetic measurement files. Computer code written to perform this step can be found at https://github.com/jeremiahws/pulse_seq_dev. The synthetic measurement files were processed in the Siemens ICE to create DICOM image files.

Dosimetric evaluation

Radioactive seed localization was performed using the 3D MRIs without coregistration or reference to a postimplant CT by 3 board-certified medical dosimetrists. All MRIs were anonymized and the dosimetrists were blinded to each other's MRIs. It is common practice to rescan patients when artifacts are present in the MRIs. This can be done when the patient is still on the table if the image reconstruction is fast and implemented on the scanner's image reconstruction computer. However, the multi-NEX acquisitions acquired with PICS required reconstructing the images offline because it was an experimental pulse sequence that was not implemented in the vendor's software. Because of this, there was no way to determine whether there were significant artifacts in the multi-NEX acquisitions until after the patient left the MRI scanner. The goal was to provide the highest quality images to the doismetrists to perform seed localization. In 5 cases in which there were artifacts present,

the higher spatial resolution MRIs were provided in place of the multi-NEX MRI. The dosimetrists used either the preplan or intraoperative plan reports to determine the needle-loading configurations and total number of seeds implanted. The dosimetrists performed the seed localization using a commercially available treatment planning system (TPS) (MIM Software Inc, Cleveland, OH) and recorded the total number of seeds they could identify and the time they required to identify them.

Image quality evaluation

Signal-to-noise ratio was measured through region of interest (ROI) analysis in 5 anatomic regions of the MRIs. Circular ROIs with an area of approximately 50 mm^2 were measured in the left obturator internus (a muscle on the left side of the prostate with a homogenous appearance on the MRIs), the peripheral zone and transition zone of the prostate, homogeneous regions within the seminal vesicles, and homogeneous regions inside the bladder.[26] Three ROI measurements were made in each anatomic region. Effort was made to place the ROIs consistently within the anatomy across acquisitions. Regions with image artifacts were avoided. Signal-to-noise ratio in each ROI was computed as the mean voxel intensity μ_{ROI} divided by the standard deviation of the voxel intensities σ_{ROI}, $SNR \approx \mu_{ROI}/\sigma_{ROI}$. The 3 SNR measurements for each anatomic region were averaged in each MRI. A detailed evaluation of the impact of the PICS reconstructions on image quality was previously retrospectively investigated in a 6-person observer study.[11]

Translation and evaluation at a community hospital

Two imaging physicists from MDACC visited PAH to provide on-site support for the initial implementation of MARS techniques using fully bSSFP at this institution. Before this, pulse sequences for planning and postimplant QA used at MDACC were transferred to PAH, and both were run on the patient for their preimplant MRI. This was the only prior experience PAH had with MARS LDR prostate brachytherapy. The day before the day of the implant, phantom testing was conducted to optimize the CISS pulse sequence for the 3T Siemens Skyra (Siemens Healthineers, Erlangen, Germany) present at the hospital. The phantom was constructed of a water-based gel and contained tissue-equivalent models of the prostate, seminal vesicles, and external urinary sphincter. The prostate phantom was implanted with dummy seeds and seed markers.

The prostate phantom was centered between 2 liquid cylindrical phantoms (Supplementary Fig. E1). An 18-channel external array coil was positioned above the phantoms and used in combination with spine coils integrated into the patient table. The CISS sequence was optimized for anatomic coverage, SNR, spatial resolution, and scan time, within the US Food and Drug Administration limit of the specific absorption ratio (SAR) computed by the scanner. Patient scanning at this institution with the accelerated sequence was not included in the Institutional Review Board-approved protocol, so the accelerated acquisitions using PICS and multi-NEX were not performed. The final pulse sequence parameters that we converged on were FOV = 15.5 × 15.5 cm, voxel size = 0.48 × 0.48 × 1.2 mm (interpolated to 0.24 × 0.24 × 1.2 mm), TR/echo time = 6.04/2.64 ms, NEX = 1, readout bandwidth = 435 Hz/pixel, flip angle = 44°, number of slices = 72 (50% slice resolution and 11.1% slice oversampling), and scan time = 4 to 6 minutes.

A 75-year-old man with confirmed prostate cancer underwent LDR prostate brachytherapy with I-125 seeds stranded with positive contrast seed markers. A total of 49 seeds were implanted. The patient was positioned using the same procedure presented in “Patient Positioning.” A board-certified medical dosimetrist with more than 25 years of experience educated the PAH medical physicists through a remote web session on how to perform postimplant seed identification in a cloud-based commercial TPS (MIM Software Inc, Cleveland, OH).

Two additional patients underwent MARS LDR prostate brachytherapy at PAH approximately 4 weeks and 10 weeks, respectively, after the first patient. Both patients were implanted with I-125 seeds stranded with positive contrast seed markers. The first additional patient was implanted with 82 seeds and the second was implanted with 80 seeds. A medical physicist at PAH performed postimplant seed identification on these 2 patients.

Results

Subjective evaluation showed that acceleration in a single phase-encoding direction with a 2-dimensional (2D) GRAPPA sampling pattern yielded the highest seed marker conspicuity (Supplementary Fig. E2) for R = 2. Additionally, including an L1 wavelet penalty into the k-space reconstruction reduced the noise amplification caused by the g-factor effect without blurring of seed markers or loss of their conspicuity (Supplementary Fig. E2, ESPIRiT vs L1-ESPIRiT). Therefore, all of the multi-NEX PICS accelerated acquisitions were performed with a 2D GRAPPA sampling pattern, with acceleration only in the phase-encoding direction, and reconstructed with L1-ESPIRiT.

Partial volume artifacts caused some of the seed markers to be unrecognizable when imaged at the moderate in-plane spatial resolution (Fig. 1A, Table 2). Increasing the in-plane spatial resolution mitigated these artifacts and improved overall seed marker detection and visualization at the expense of reduced SNR (Fig. 1C vs 1A, Table 2).

Figure 2 shows a comparison of fully sampled acquisitions and multi-NEX acquisitions accelerated with PICS at the moderate and high in-plane spatial resolutions. At the moderate in-plane spatial resolution, acquiring images with 3 NEX and R = 2 showed improvements in SNR compared with that in the fully sampled image with NEX = 1 in approximately 6 minutes of scan time (Fig. 2A vs Fig. 2B, Table 2). However, even with high SNR, partial volume artifacts caused the boundaries of the seed markers to be blurred. The sharpness and overall conspicuity of the seed markers was improved by increasing the in-plane spatial resolution at the expense of reduced SNR (Fig. 2B vs Fig. 2C, Table 2). Acquiring images with NEX = 2 and R = 2 at high in-plane spatial resolution maintained the sharpness of the seed markers and produced an increase in the SNR (Fig. 2C vs Fig. 2D, Table 2). MRIs from 6 additional patients acquired at high and very high in-plane spatial resolutions with multiple NEX are shown in Supplementary Figures E6 to E11.

A total of 1214 radioactive seeds were implanted in the 17 patients at PAH whose MRIs were evaluated. Table 3 summarizes the radioactive seed counts from the evaluation by 3 certified medical dosimetrists. Dosimetrist 1 identified all of the radioactive seeds with

perfect precision and recall in 15 patients. This dosimetrist also reported an area in the anterior peripheral zone where 2 seed strands were crossing in patient 1, leading to identification of 1 false positive. In patient 15, this dosimetrist also reported that 2 strands placed in proximity made 1 seed unidentifiable, a false negative (FN). Average time to identify the seeds for dosimetrist 1 was 18.2 ± 8.5 minutes per patient (mean ± 1 standard deviation). In total, dosimetrist 1 identified 1214 seeds in 310 minutes (3.9 seeds/min). Dosimetrist 2 had perfect precision and recall in identification of the radioactive seeds for 15 of the 17 patients. In patient 4, dosimetrist 2 was not able to locate 1 of the implanted markers that separated 2 seeds. Although dosimetrist 2 was able to identify the signal voids of the seeds, they were clustered with other signal voids near the peripheral zone, resulting in failure to identify 2 seeds, 2 FNs. They also had the same issue as dosimetrist 1 for failing to identify 1 seed, a FN, in patient 15. Their average time to identify the seeds was 38.7 ± 11.3 minutes per patient. Dosimetrist 2 identified a total of 1211 seeds in 658 minutes (1.8 seeds/min). Dosimetrist 3 had perfect precision and recall for all 17 of the patients. Their average time per patient was the highest of the 3 at 39.3 ± 13.5 minutes per patient. Dosimetrist 3 identified all 1214 seeds in 662 total minutes (1.8 seeds/min).

Figure 3 shows postimplant MRIs at 3 spatial resolutions of a patient with a height of 5’9” and weight of 312 pounds. This patient barely fit into the scanner bore and demonstrates the upper limit of the challenges faced for post-implant MRI without an ERC. Although the moderate in-plane spatial resolution had the highest SNR of the 3 MRIs (Fig. 3A, Table 2), comparison with the MRIs at the 2 higher in-plane spatial resolutions (Fig. 3B and 3C, Table 2) revealed seed markers that were undistinguishable in the moderate in-plane spatial resolution MRI. Acquiring multi-NEX acquisitions likely would have improved the SNR in the 2 higher in-plane spatial resolution scans, but the patient became uncomfortable after the first 3 MRIs, so we aborted the additional scans using multi-NEX PICS acquisitions. Nevertheless, all 3 dosimetrists identified all of the implanted radioactive seeds in this patient (patient 17 in Table 3) without reference to a postimplant CT.

Example views of the postimplant MRI acquired of the first prostate cancer patient treated with MARS using LDR brachytherapy at PAH are shown in Figure 4 (Supplementary Fig. E13 shows multiple axial slices of the same patient). Excellent delineation of the prostatic capsule was observed, along with the surrounding normal anatomic structures (urinary bladder base, rectum, mesorectum, and pelvic floor). Furthermore, the seed markers and radioactive seeds were adequately visualized, enabling identification of all 49 of the implanted seeds for postimplant dosimetry. Supplementary Figures E14 to E15 show MRIs of the second and third patients treated at PAH. For the second patient, 81/82 of the implanted seeds were identified on the MRI without reference to CT. One seed on the left posterior border of the prostate could not be identified (a FN) in the MRI because the signal void of the seed blended in with the surrounding anatomy; reference to postimplant CT was required for the medical physicist to find this remaining seed. For the third patient, 78/80 of the implanted seeds were identified on the MRI without reference to CT. One strand containing 2 seeds with a seed marker in between them was implanted outside the right side of the prostate and could not be identified (2 FNs); the medical physicist had to refer to a postimplant CT to identify where this strand was implanted. The MRIs from these additional

2 patients were reviewed by the more experienced medical dosimetrist from MDACC, and she reported she could identify the FNs that were missed.

Discussion

Acquiring high-quality postimplant MRIs without an ERC has several advantages including improved patient tolerance, reduced cost, higher clinical throughput, and greater accessibility to MARS LDR prostate brachytherapy for community practices. The feasibility of using PICS to accelerate postimplant prostate brachytherapy MRIs was previously demonstrated retrospectively.[11] In the present study, we confirmed the feasibility of this approach in the context of prospective clinical patient imaging. We acquired high and very high in-plane spatial resolution images using a total scan time between 4 and 6 minutes each, demonstrating the practicality of this technique for integration into routine clinical workflows. Furthermore, multi-NEX acquisitions enabled by PICS provided improved SNR compared with fully sampled acquisitions acquired with 1 NEX. As such, combining PICS with fully bSSFP enables high spatial resolution and high SNR for MARS without an ERC.

Previously, the impact of imaging without an ERC on the ability to identify radioactive seeds in 5 prostate cancer patients treated with MARS LDR brachytherapy was investigated.[27] The results demonstrated that compared with imaging with an ERC, imaging without one at 1.5T and with moderate in-plane spatial resolution (0.586 × 0.586 mm, interpolated to 0.293 × 0.293 mm) caused a reduction in radioactive seed recall of 43.5 ± 31.1% and increase in the time required to perform seed identification of 57.2 ± 67.3%. In the present study imaging without an ERC, the 3 certified medical dosimetrists achieved near perfect precision and recall in identification of the radioactive seeds in the 17 patients without the use of CT using the high/very high spatial resolution MRIs.

Since 2016, moderate spatial resolution acquisitions using fully bSSFP have been acquired at 1.5T and with an ERC for postimplant QA of MARS LDR prostate brachytherapy.[8] However, uncertainty in the precise location of some radioactive seeds would arise clinically, leading to dosimetrists requiring fusion of postimplant CT with the postimplant MRI for identification of the inconspicuous seeds and seed markers. In the present study, we demonstrated that imaging at higher in-plane spatial resolutions improved the conspicuity of the implanted seed markers for subsequent seed localization. By reducing the in-plane voxel size, partial volume artifacts were reduced and finer spatial details were resolved. We showed that through gradual reductions in the in-plane voxel size, seed markers that were previously inconspicuous became well visualized by the human eye. However, reducing the voxel size comes with an associated reduction in SNR. In situations in which the SNR is limited, multi-NEX acquisitions with PICS can be used as a strategy to boost the SNR without significantly increasing the scan time.

Although we demonstrated that postimplant seed identification can be performed without the use of postimplant CT, instances may still arise in which a postimplant CT is required. One primary limitation of MRI is motion artifacts caused by contaminated phase-encoding lines in the sampled k-space data. Although accelerated scanning with PICS can help manage motion artifacts by reducing the time latency of the acquisition, instances can still arise

clinically where they are unavoidable. For example, in the present study we encountered 2 patients with restless legs syndrome who could not control their leg movements during their MRI. This produced substantial motion artifacts, causing many of the radioactive seeds and seed markers to become significantly blurred and unrecognizable. When such scenarios arise, a postimplant CT may be required to perform postimplant QA with confidence.

In addition to being the first prospective report of postimplant MRI for MARS LDR prostate brachytherapy without an ERC, this study is the first to describe translation of these advanced MRI techniques from a major academic center to the community setting. Although the PICS acquisitions were not performed at the community hospital, imaging at high in-plane spatial resolution proved to be sufficient for postimplant seed localization. With guidance from an expert certified medical dosimetrist, the medical physicists at PAH identified all of the implanted radioactive seeds using a commercial TPS for postimplant QA for the first patient treated at PAH. Almost all of the radioactive seeds in the second and third patients were identified (81 of 82 and 78 of 80, respectively) without reference to CT independently by the medical physicists at PAH. More experience with MRI-based postimplant assessment is expected to improve the medical physicists' seed localization ability. This strategy translating postimplant QA for MARS LDR prostate brachytherapy to a new hospital may serve as a model to improve access to MARS in the community setting.

We reconstructed the k-space data for the accelerated acquisitions using BART and a fast iterative shrinkage-thresholding optimization algorithm incorporated in BART. Researchers have validated BART in a number of MRI studies across multiple MRI applications, and the developers of compressed sensing for MRI and the ESPIRiT parallel imaging technique develop and maintain BART. Recently, several studies have demonstrated the feasibility of using deep machine learning techniques for reconstructing accelerated MRI scans without significant degradations in image quality. These techniques present the potential opportunity to increase acceleration factors for PICS acquisitions for MARS LDR prostate brachytherapy without compromising image quality. Future studies investigating deep machine learning for accelerated prostate brachytherapy MRIs could be beneficial for faster imaging and multi-NEX acquisitions.

Our use of 2D GRAPPA sampling patterns deviates from the traditional Poisson-disk sampling patterns used for CS reconstructions. The sampling densities for 2D GRAPPA patterns are constant in both the low and high frequency regions of k-space (aside from the autocalibration region, which is fully sampled). In contrast, the sampling densities for Poisson-disk patterns fall off toward the edges of k-space, which is where the high frequency content of the MRIs is contained. The objects of interest (seeds and seed markers) are small and contain significant high-frequency components, which could be the reason the 2D GRAPPA sampling patterns yield slightly higher seed marker conspicuity for $R = 2$.

In translation of MARS LDR prostate brachytherapy from a major academic center to the community hospital, we experienced and highlighted some considerations that should be made when implementing fully bSSFP in the clinic. One is that the ability to optimize the CISS sequence partly depends on the scanner hardware installed. The Skyra scanner at the community hospital did not have as powerful a gradient package as the Prisma scanner at

MDACC with which we originally developed these techniques. Therefore, we were limited to scanning at only moderate and high in-plane spatial resolutions. Nevertheless, high in-plane spatial resolution still provided adequate visualization of the implanted seed markers. A second consideration was that the SAR calculations on the Skyra MRI scanner, which are performed to comply with US Food and Drug Administration regulations, limit the range of pulse sequence parameters that can be selected. Using a high flip angle (as close as possible to 90°) with fully balanced SSFP is desirable to gain more signal and positive contrast from the seed markers[15] but comes with an increase in the SAR, so we were limited in the value of the flip angle we could select. Reducing the number of phase- and/or slice-encoding lines is a potential strategy for reducing the net energy absorbed in the patient but may restrict the spatial coverage and spatial resolution to ranges that negatively affect the ability to perform postimplant QA. Using low SAR flip angles is an additional strategy for reducing the SAR, but it comes with an increase in scan time and susceptibility to banding artifacts.

The prostate can have a heterogeneous appearance in the fully bSSFP MRIs (eg, see Fig. 2), including both regions of hypointensity and hyperintensity. Because the radioactive seeds appear as small regions of hypointensity, and the seed markers appear as small regions of hyperintensity, the seeds and markers may appear to blend in with these heterogenous regions if implanted adjacent to them. However, the seeds and markers were implanted using a stranded technique, which allows the dosimetrists to follow the strands along the craniocaudal dimension and aid with seed and marker identification in these regions of potential uncertainty. Additionally, the active diameter of the markers is only 0.5 mm; the material encapsulating the marker contrast solution produces a ring of negative contrast around the active diameter of the markers. This feature of the seed markers further aids in their identification, including near regions of hyperintensity in the prostate.

Seeds are often implanted in extraprostatic regions of the prostate, either intentionally because of a dosimetric advantage, or resulting from slight geometric errors during the manual implant procedure causing some seeds to be offset from their planned locations. When these extraprostatic seeds are near the anatomic boundary of the prostate, they could appear less conspicuous because of regions of heterogeneous negative contrast along the prostate boundary masking the seeds. The 3 dosimetrists from MDACC, who all have significant experience with MRI-based postimplant assessment, did not report any issues identifying seeds implanted in extraprostatic zones of the 17 patients they analyzed. However, the medical physicist at PAH reported 1 FN from their second patient and 2 FNs from their third patient, which were all seeds that were implanted in extraprostatic regions. Thus, more experience with MRI-based postimplant assessment may lead to improvements in identifying extraprostatic seed implants.

Another group recently investigated MRI for postimplant imaging in LDR prostate brachytherapy.[28] Their approach relies on acquiring an anatomic T2-weighted MRI for anatomic delineation and a multiecho gradient recalled echo (GRE) MRI to estimate quantitative susceptibility maps for seed identification. This requires coregistration between the 2 MRIs for postimplant dosimetry. By comparison, our approach requires only a single acquisition to visualize the prostate, surrounding organs at risk, and the implanted radioactive seeds, which avoids the need for coregistering multiple MRIs. Moreover, our

approach requires only ~4 to 6 minutes compared with the ~10 minutes required for the multiecho GRE (which is highly prone to motion artifacts owing to the long acquisition time) plus the additional scan time for the T2-weighted anatomic MRI used by Nosrati et al.[28]

A prior work investigated automatic seed localization in fully bSSFP MRIs acquired at 1.5T with moderate spatial resolution and without an ERC.[29] That work demonstrated good recall of the radioactive seeds but only moderate precision of 90% across 20 test patients. Because of the inherently lower SNR, several false positives were produced owing to the poor visualization of the seed markers. The present work demonstrated improved seed marker visualization and overall image quality without using an ERC through pulse sequence optimization. The improvements in image quality may improve the precision of automated MRI-based seed detection algorithms and would be interesting to investigate in future work.

This study has some limitations. One is that we have only reported results for 3T MRI. Many hospitals, both in the academic and community settings, have 1.5T MRI scanners. Differences in the static magnetic field strength can influence MR image quality and the ability to visualize radioactive seeds, seed markers, and relevant anatomic structures. The SAR is also proportional to the square of the magnetic field strength, so more flexibility in optimizing scanning protocols with respect to SAR may be available when imaging at 1.5T (eg, higher flip angles could potentially be used). Future studies imaging without an ERC at 1.5T using the techniques proposed herein are needed to determine their clinical applicability at that field strength. A second limitation is that we present imaging results for only 3 patients at the community hospital. Although MARS LDR prostate brachytherapy has become the standard of practice at MDACC, it is just beginning at PAH. The purpose of including these 3 patients in this study was not to draw statistical conclusions from them, but rather to demonstrate the feasibility of translating some of the MRI techniques that were presented to a community setting for the first time. PAH now uses fully balanced SSFP for postimplant quality assessment, and comprehensive statistical analyses, if necessary, could be performed in the future when PAH has treated more prostate patients with LDR brachytherapy and accumulated more patient images. A third limitation is that the MRI techniques studied in this work were for use with implanted positive contrast seed markers in addition to anatomic imaging.

Conclusion

This prospective study confirmed the feasibility of combining PICS with fully bSSFP to improve SNR within a comparable total scan time through multi-NEX acquisitions. Although this technique may not be required for MRI of some patients, we demonstrated how this technique could be used in scenarios in which the SNR is lower without significantly increasing the scan time (eg, when imaging at 1.5T instead of 3T). We also demonstrated that high in-plane spatial resolution improved the conspicuity of the implanted seed markers for subsequent localization of the radioactive seeds. With the high in-plane spatial resolution acquisitions, 3 medical dosimetrists identified the implanted radioactive seeds in 17 patients with nearly perfect precision and recall, giving confidence in the potential omission of postimplant CT for future patient treatments with MARS LDR prostate

brachytherapy. Furthermore, we describe, for the first time, the implementation of postimplant QA for MARS LDR prostate brachytherapy without an ERC at a community hospital. This experience offers the prospect of expanded access of MARS LDR brachytherapy to the broader community setting.

Supplementary Material

Refer to Web version on PubMed Central for supplementary material.

Acknowledgments—

J.W.S. would like to acknowledge the donors of the Pauline Altman-Goldstein Foundation Discovery Fellowship. The authors would like to acknowledge Scientific Publications, Research Medical Library at the University of Texas MD Anderson Cancer Center for professionally editing this paper.

J.W.S. was supported by a fellowship from the Pauline Altman-Goldstein Foundation. J.W.S. was also partially supported by a sponsored research grant from Siemens Healthineers. This study was supported by the NIH/NCI under award number P30CA016672.

References

1. Brinkmann DH, Kline RW. Automated seed localization from CT datasets of the prostate. Med Phys 1998;25:1667–1672. [PubMed: 9775371]
2. Christodouleas J, Fox J, Song D, et al. Basic terms and concepts of radiation In: Su L-M, editor. Early Diagnosis and Treatment of Cancer Series: Prostate Cancer. Philadelphia: WB Saunders; 2010 p. 159–175.
3. Nitz WR, Reimer P. Contrast mechanisms in MR imaging. Eur Radiol 1999;9:1032–1046. [PubMed: 10415233]
4. Amdur RJ, Gladstone D, Leopold KA, et al. Prostate seed implant quality assessment using MR and CT image fusion. Int J Radiat Oncol Biol Phys 1999;43:67–72. [PubMed: 9989515]
5. De Brabandere M, Al-Qaisieh B, De Wever L, et al. CT- and MRI-based seed localization in postimplant evaluation after prostate brachytherapy. Brachytherapy 2013;12:580–588. [PubMed: 23876358]
6. Crook J, McLean M, Yeung I, et al. MRI-CT fusion to assess post-brachytherapy prostate volume and the effects of prolonged edema on dosimetry following transperineal interstitial permanent prostate brachytherapy. Brachytherapy 2004;3:55–60. [PubMed: 15374536]
7. Polo A, Cattani F, Vavassori A, et al. MR and CT image fusion for postimplant analysis in permanent prostate seed implants. Int J Radiat Oncol Biol Phys 2004;60:1572–1579. [PubMed: 15590189]
8. Ma J, Moerland MA, Venkatesan AM, et al. Pulse sequence considerations for simulation and postimplant dosimetry of prostate brachytherapy. Brachytherapy 2017;16:743–753. [PubMed: 28063817]
9. Frank SJ, Stafford RJ, Bankson JA, et al. A novel MRI marker for prostate brachytherapy. Int J Radiat Oncol Biol Phys 2008; 71:5–8. [PubMed: 18406882]
10. Frank SJ, Johansen MJ, Martirosyan K, et al. A biodistribution and toxicity study of cobalt dichloridee–N-acetyl cysteine (C4) as an implantable MRI marker for prostate cancer treatment. Int J Radiat Oncol Biol Phys 2013;85:1024–1030. [PubMed: 23092727]
11. Sanders JW, Song H, Frank SJ, et al. Parallel imaging compressed sensing for accelerated imaging and improved signal-to-noise ratio in MRI-based postimplant dosimetry of prostate brachytherapy. Brachytherapy 2018;17:816–824. [PubMed: 29880449]
12. Lim TY, Stafford RJ, Kudchadker RJ, et al. MRI characterization of cobalt dichloride-N-acetyl cysteine (C4) contrast agent marker for prostate brachytherapy. Phys Med Biol 2014;59:2505–2516. [PubMed: 24778352]

13. Lim TY, Kudchadker RJ, Wang J, et al. Development of a magnetic resonance imaging protocol to visualize encapsulated contrast agent markers in prostate brachytherapy recipients: initial patient experience. J Contemp Brachytherapy 2016;8:235–242. [PubMed: 27504133]
14. Lim TY, Kudchadker RJ, Wang J, et al. Effect of pulse sequence parameter selection on signal strength in positive-contrast MRI markers for MRI-based prostate postimplant assessment. Med Phys 2016;43:4312–4322. [PubMed: 27370146]
15. Bieri O, Scheffler K. Fundamentals of balanced steady state free precession MRI. J Magn Reson Imaging 2013;38:2–11. [PubMed: 23633246]
16. Chavhan GB, Babyn PS, Jankharia BG, et al. Steady-state MR imaging sequences: Physics, classification, and clinical applications. Radiographics 2008;28:1147–1160. [PubMed: 18635634]
17. Lustig M, Donoho D, Pauly JM. Sparse MRI: The application of compressed sensing for rapid MR imaging. Magn Reson Med 2007;58: 1182–1195. [PubMed: 17969013]
18. Lustig M, Pauly JM. SPIRiT: Iterative self-consistent parallel imaging reconstruction from arbitrary k-space. Magn Reson Med 2010;64:457–471. [PubMed: 20665790]
19. Murphy M, Alley M, Demmel J, et al. Fast l_1-SPIRiT compressed sensing parallel imaging MRI: Scalable parallel implementation and clinically feasible runtime. IEEE Trans Med Imaging 2012;31:12501262.
20. Griswold MA, Jakob PM, Heidemann RM et al. Generalized autocalibrating partially parallel acquisitions (GRAPPA). Magn Reson Med. 47:1202–1210.
21. Uecker M. Toolbox for computational magnetic resonance imaging. Available at: https://mrirecon.github.io/bart/. Accessed August 15, 2019.
22. Uecker M, Ong F, Tamir JI, et al. Berkeley advanced reconstruction toolbox. Proc Intl Soc Mag Reson Med 2015;23:2486.
23. Tamir JI, Ong F, Cheng JY, et al. Generalized magnetic resonance image reconstruction using the Berkeley advanced reconstruction toolbox. Proc Intl Soc Mag Reson Med 2016.
24. Ehses P. mapVBVD. Available at: https://github.com/CIC-methods/FID-A/tree/master/inputOutput/mapVBVD. Accessed August 15, 2019.
25. Uecker M, Lai P, Murphy MJ, et al. ESPIRiT–An eigenvalue approach to autocalibrating parallel MRI: Where SENSE meets GRAPPA. Magn Reson Med 2014;71:990–1001. [PubMed: 23649942]
26. Bathala TK, Venkatesan AM, Ma J, et al. Quality comparison between three-dimensional T2-weighted SPACE and two-dimensional T2-weighted turbo spin echo magnetic resonance images for the brachytherapy planning evaluation of prostate and periprostatic anatomy. Brachytherapy 2020;19:484–490. [PubMed: 32402544]
27. Sanders J, Frank S, Bathala T, et al. MRI-based prostate brachytherapy-imaging with and without an endorectal coil for post-implant quality assurance. Brachytherapy 2016;16:S56.
28. Nosrati R, Wronski M, Tseng CL, et al. Postimplant dosimetry of permanent prostate brachytherapy: Comparison of MRI-only and CT-MRI fusion-based workflows. Int J Radiat Oncol Biol Phys 2020; 106:206–215. [PubMed: 31627178]
29. Sanders JW, Frank SJ, Kudchadker RJ, et al. Development and clinical implementation of SeedNet: A sliding-window convolutional neural network for radioactive seed identification in MRI-assisted radiosurgery (MARS). Magn Reson Med 2019;81:3888–3900. [PubMed: 30737827]

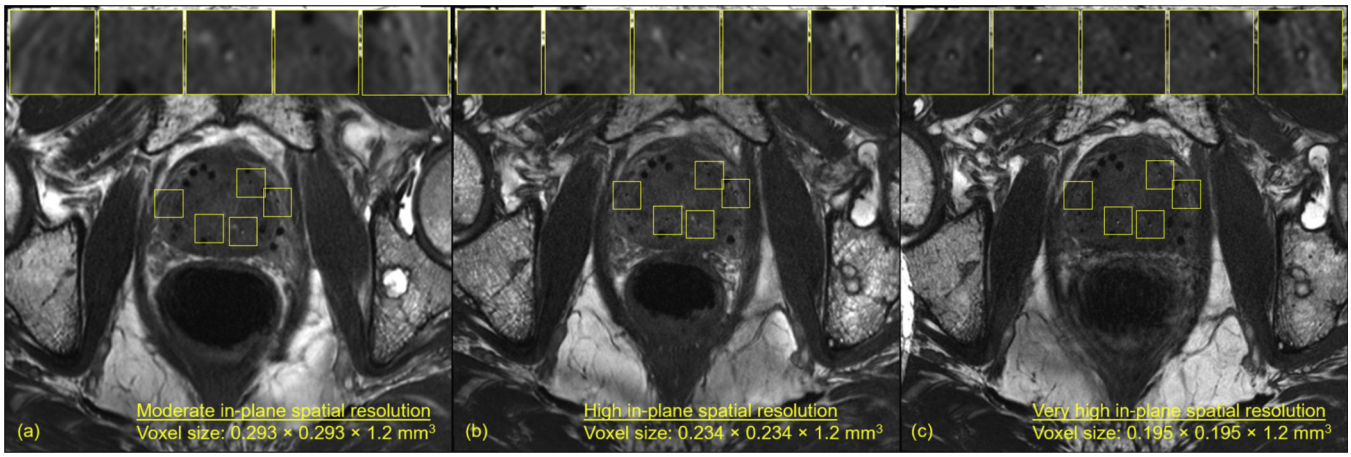

Fig. 1.

Magnetic resonance imaging of the same patient acquired at (A) moderate in-plane spatial resolution, (B) high in-plane spatial resolution, and (C) very high in-plane spatial resolution. Some markers that were undetectable at the moderate in-plane spatial resolution became well visualized at the high and very high in-plane spatial resolutions. (B) and (C) were acquired approximately 30 minutes after (A). In between the acquisitions, the patient moved his left leg, causing the location of the bone metastasis in (B) and (C) to be offset approximately 3 slices (~3.6 mm) from its anatomic location shown in (A). The axials slices shown are of the same anatomic location in the patient's prostate. Additional axial slices from all 3 magnetic resonance imagings in (A-C) can be viewed in Supplementary Figures E3 to E5.

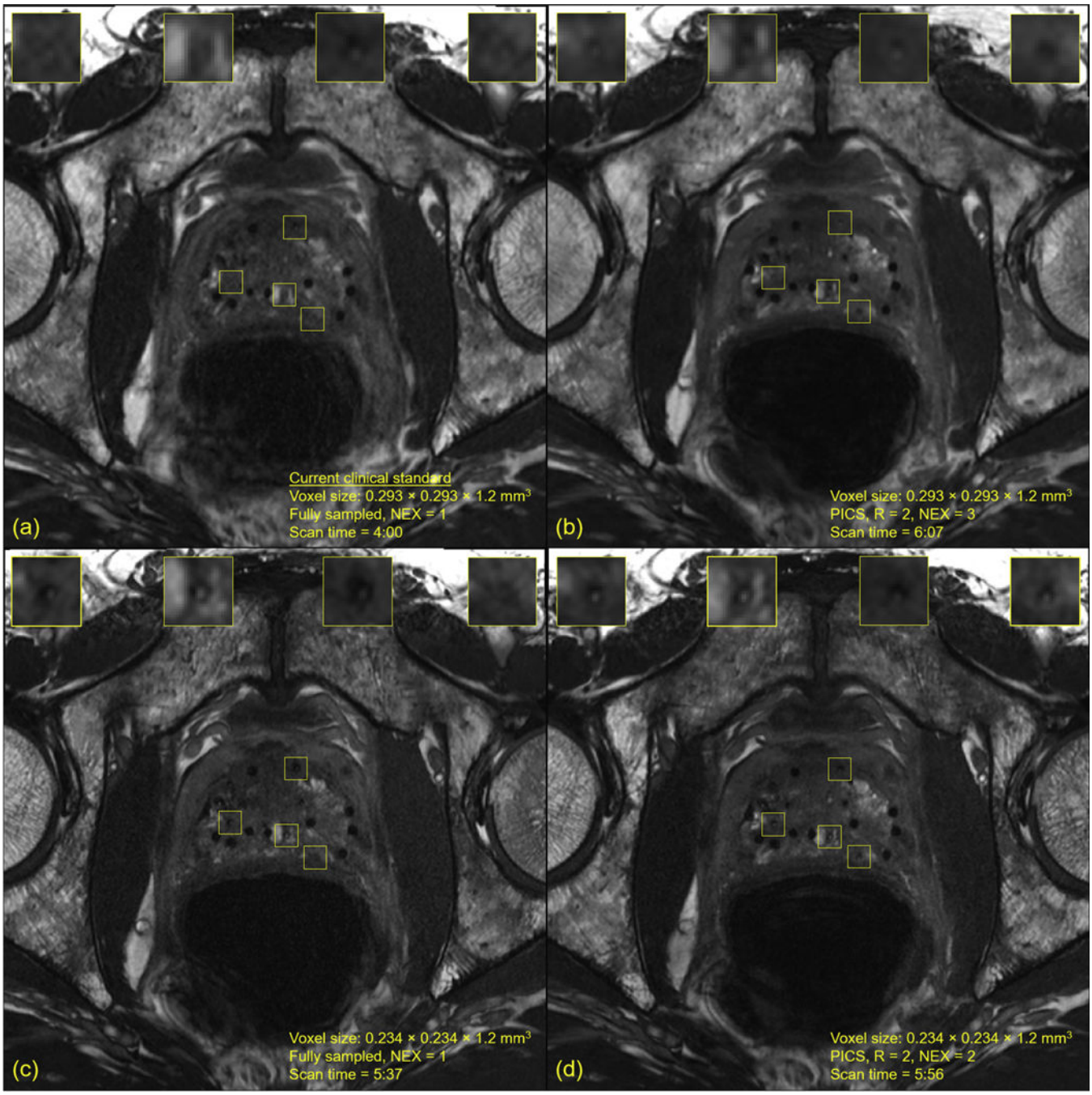

Fig. 2.

Magnetic resonance imaging (MRI) of the same patient imaged with multiple in-plane spatial resolutions and accelerated signal averages. Supplementary Figure E12 compares 1 strand in a sagittal view in normal magnification across the 4 acquisitions. (A) Fully sampled constructive interference in steady-state (CISS) MRI acquired at the moderate in-plane spatial resolution, which is the current clinical standard. (B) Accelerated CISS MRI acquired at the moderate in-plane spatial resolution, R = 2, number of signal averages = 3, and reconstructed with parallel imaging and compressed sensing. A notable increase in

signal to noise was achieved compared with (A). (C) Fully sampled CISS MRI acquired at the high in-plane spatial resolution. Increased visualization of the implanted seed markers was achieved compared with that in (A). (D) Accelerated CISS MRI acquired at the high in-plane spatial resolution, R = 2, number of signal averages = 2, and reconstructed with parallel imaging and compressed sensing. An improvement in signal to noise was achieved compared with that in (C). These 4 MRIs are consecutive acquisitions of the same patient; because of the small voxel sizes, slight interscan patient motion may have caused minor shifts in anatomic landmarks, potentially causing slight differences in appearance of the seed markers.

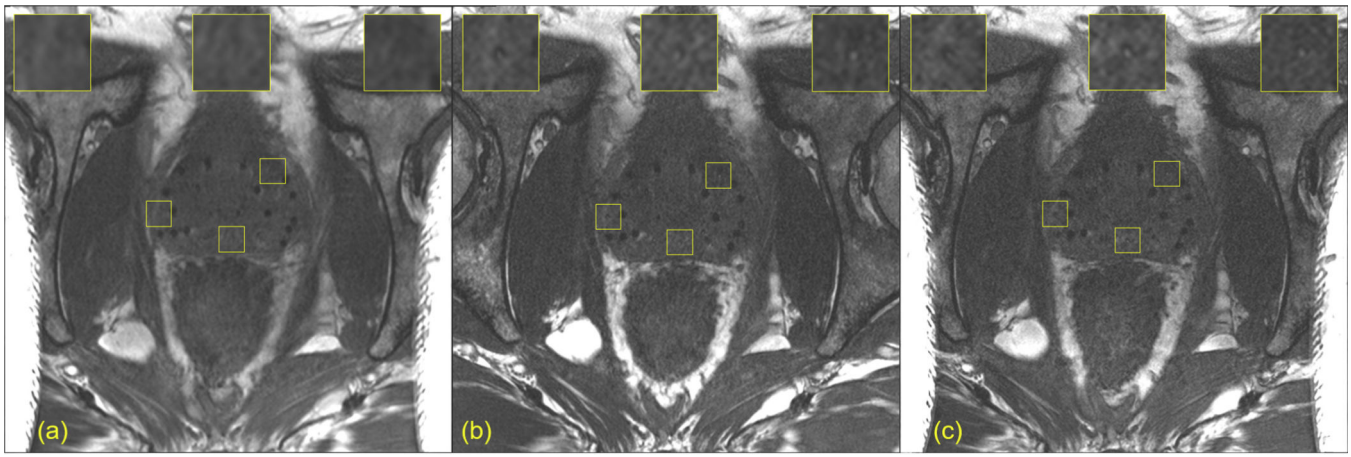

Fig. 3.

Axial views of postimplant magnetic resonance imaging of a large patient obtained at increasing in-plane spatial resolutions. (A) Moderate in-plane spatial resolution. (B) High in-plane spatial resolution. (C) Very high in-plane spatial resolution.

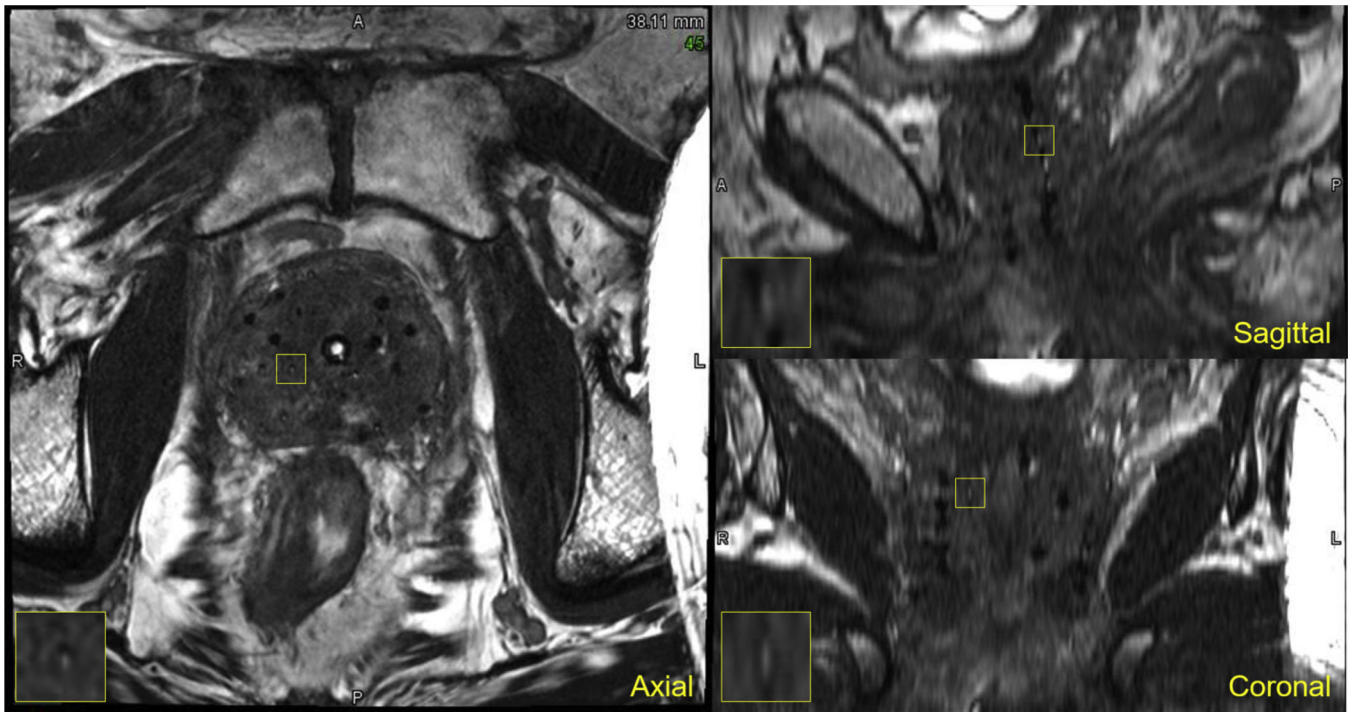

Fig. 4.

Multiplanar views of a postimplant magnetic resonance imaging of the first patient at the community hospital implanted with magnetic resonance−signal producing seed markers and imaged using fully balanced steady-state free precession.

Table 1

Typical pulse sequence parameters used for the postimplant MRIs

	Moderate resolution	High resolution	Very high resolution
Field of view, cm	15 × 15	15 × 15	15 × 15
Slice thickness, mm	1.2	1.2	1.2
Slice resolution, oversampling, %	50, 11.1	50, 11.1	50, 11.1
No. of slices	72	72	72
Nx	256	320	384
Phase resolution, oversampling, %	100, 100	100, 100	90, 80
TR/TE, ms	5.25/2.28	5.99/2.61	6.62/2.82
Flip angle	43°	39°	41°
Bandwidth, Hz/pixel)	590	473	395
NEX	1, 3	1, 2	1, 2
Acceleration factor	1, 2	1, 2	1, 2
Scan time, min:s	4:00, 6:07	5:08, 5:20	5:31, 5:44

Abbreviations: NEX = number of signal averages; Nx = number of frequency encoding steps; TE = echo time; TR = repetition time.

Phase- and slice-encoding parameters could have slightly changed on a patient-specific basis to ensure adequate anatomic coverage with minimal phase wrap.

Table 2

SNR measurements from the patient MRIs shown in Figures 1 to 3

Figure	Spatial resolution	NEX	PZ SNR	TZ SNR	SV SNR	Bladder SNR	Left OI SNR
1A	MR	1	8.03 ± 1.74	10.30 ± 2.08	6.09 ± 0.33	26.59 ± 3.17	8.98 ± 0.98
1B	HR	1	7.06 ± 1.64	9.63 ± 2.03	5.31 ± 0.60	18.69 ± 3.36	7.77 ± 0.66
1C	VHR	1	5.14 ± 1.37	8.27 ± 1.22	4.96 ± 0.52	11.32 ± 2.24	6.52 ± 0.25
2A	MR	1	4.78 ± 1.24	6.55 ± 1.29	7.27 ± 2.14	27.63 ± 3.30	9.87 ± 1.44
2B	MR	3	5.74 ± 2.75	9.05 ± 2.12	9.71 ± 2.85	41.32 ± 5.83	13.88 ± 2.08
2C	HR	1	4.13 ± 1.46	6.45 ± 1.27	5.75 ± 1.21	20.87 ± 1.49	8.77 ± 1.51
2D	HR	2	5.54 ± 3.65	7.76 ± 1.01	8.73 ± 3.63	26.08 ± 3.28	8.62 ± 1.06
3A	MR	1	8.31 ± 1.14	7.68 ± 0.89	5.59 ± 1.03	9.27 ± 0.92	7.00 ± 0.47
3B	HR	1	5.22 ± 0.87	4.69 ± 0.20	4.06 ± 0.44	5.42 ± 0.33	4.12 ± 0.53
3C	VHR	1	4.54 ± 0.31	4.28 ± 0.27	4.29 ± 0.29	5.63 ± 0.42	3.56 ± 0.10

Abbreviations: HR = high spatial resolution; MR = moderate spatial resolution; NEX = number of signal averages; OI = obturator internus; PZ = peripheral zone; SNR = signal to noise; SV = seminal vesicles; TZ = transition zone; VHR = very high spatial resolution.

SNR was measured in the bladder. Measurements are reported as mean ± 1 standard deviation.

Table 3

Summary of seed identification in the postimplant MRIs acquired without an ERC for the 3 medical dosimetrists

	Dosimetrist 1					Dosimetrist 2				Dosimetrist 3			
Patient	**Seeds implanted**	**Seeds found**	**Time (min)**	**P (%)**	**R (%)**	**Seeds found**	**Time (min)**	**P (%)**	**R (%)**	**Seeds found**	**Time (min)**	**P (%)**	**R (%)**
1	99	100	39	99	100	99	50	100	100	99	75	100	100
2	68	68	19	100	100	68	32	100	100	68	36	100	100
3	46	46	10	100	100	46	22	100	100	46	32	100	100
4	50	50	15	100	100	48	27	100	96	50	30	100	100
5	76	76	20	100	100	76	39	100	100	76	48	100	100
6	93	93	20	100	100	93	52	100	100	93	42	100	100
7	50	50	10	100	100	50	25	100	100	50	20	100	100
8	40	40	9	100	100	40	20	100	100	40	17	100	100
9	75	75	18	100	100	75	47	100	100	75	35	100	100
10	89	89	17	100	100	89	43	100	100	89	37	100	100
11	50	50	11	100	100	50	29	100	100	50	37	100	100
12	70	70	13	100	100	70	38	100	100	70	35	100	100
13	80	80	14	100	100	80	44	100	100	80	45	100	100
14	86	86	19	100	100	86	52	100	100	86	44	100	100
15	99	98	37	100	99	98	57	100	99	99	60	100	100
16	72	72	16	100	100	72	42	100	100	72	39	100	100
17	71	71	23	100	100	71	39	100	100	71	30	100	100
Total	1214	1214	310	-	-	1211	658	-	-	1214	662	-	-

Abbreviations: ERC = endorectal coil; P = precision; R = recall.